Assessment of geometrically necessary dislocation levels derived by 3D EBSD

P.J. Konijnenberg [a,b,*], S. Zaefferer [a], D. Raabe [a]

[a] Max-Planck-Inst. für Eisenforschung, Max-Planck-Str 1, 40237 Düsseldorf, Germany
[b] Bruker Nano GmbH, Am Studio 2D, 12489 Berlin, Germany

ABSTRACT

Existing alternatives for the calculation of geometrically necessary dislocation (GND) densities from orientation fields are discussed. Importantly, we highlight the role of reference frames and consider different sources of error. A well-controlled micro cantilever bending experiment on a copper bicrystal has been analyzed by 3-dimensional electron back scatter diffraction (3D EBSD). The GND density is determined experimentally by two different approaches and assessed theoretically, assuming a homogeneous bending of the cantilever. Experiment and theory agree very well. It is further shown that the deformation is accommodated mainly by GNDs, which carry and store lattice rotation, and not (only) by mobile dislocations that leave a crystal portion inspected, without lattice rotations. A detailed GND analysis reveals a local density minimum close to the grain boundary and a distinct difference in edge to screw ratios for both grains.

1. Introduction

Stored dislocations are generally divided into geometrically necessary dislocations (GNDs), which accommodate a lattice curvature from a deformation gradient, and statistically stored dislocations (SSDs), which accumulate due to statistical entanglements. The focus of this work is entirely on the class of GNDs. As GNDs are the result of a deformation process, they are mainly a measure for differences in plastic flow and they contribute to the stored energy and strain hardening during cold working.

Nye [1], Kröner [2,3] and Bilby et al. [4] established a continuum dislocation theory that provides the connection between the lattice curvature and a continuous GND distribution. Sun et al. [5] were the first to apply this theory with the help of electron backscatter diffraction (EBSD) to resolve GND distributions in Al bicrystals. Since then, a range of studies into GND distributions have been performed, all based on employing conventional EBSD pattern analysis by Hough transform [6–12]. More recently, EBSD pattern cross correlation has been applied to obtain more accurate lattice rotation and GND results, [13–19]. As most GND studies are based on 2-dimensional EBSD measurements, they consequently deal with the missing out-of-plane components in Nye's dislocation tensor in various ways. Recent advancements, by solving an additional static stress equilibrium condition, have led to a complete (but still surface based) dislocation tensor, though [20]. The current work is entirely based on 3D EBSD measurements and therefore neither limited by an incomplete Nye tensor nor by a missing dimension in the GND density field. Our 3D EBSD measurements are performed by serial sectioning with a focussed Ga^+-ion beam and a subsequent mapping of the consecutive sections by EBSD.

The number of methods to map dislocation densities by other means is rather limited and includes methods such as direct observations by electron channelling contrast imaging (ECCI) and transmission electron microscopy or indirect observations by etch pits or X-ray diffraction profile analysis. This and the difficulty to differentiate between GNDs and SSDs is probably the main reason why there have been only very few attempts so far to compare the outcome of GND calculations with direct measurements of dislocation densities, [21].

In the present work we attempt to verify the density of GNDs obtained by 3D EBSD on the basis of an experiment which creates an analytically quantifiable amount of GNDs. We use a constrained micro-cantilever bending experiment, assuming that the GND density can be calculated from an experimentally determinable bending radius. Provided that the deformation is carried mainly by GNDs, this will be a suitable set-up to relate GND densities to the plastic deformation gradient, [22].

* Corresponding author at: Max-Planck-Inst. für Eisenforschung, Max-Planck-Str 1, 40237 Düsseldorf, Germany.

E-mail address: p.konijnenberg@mpie.de (P.J. Konijnenberg).

Only few micro-beam bending experiments have been documented in literature and they are essentially devoted to measuring continuum properties of the beams. Crystal bending was studied by Stölken et al. [23] on Ni polycrystalline thin films. They reported a size-dependent strength and strain hardening. In two studies by Demir et al. [24,25], size dependent yield stress values were observed during bending of monocrystalline cantilever beams and shear localizations were mapped by EBSD. In a similar cantilever bending experiment, conducted on single crystalline copper, the same authors observed a Bauschinger effect, [26].

The outline of this paper is as follows. In section 2 we revisit the calculation of geometrically necessary dislocation densities from orientation data. We address some important details as well as alternative possibilities to extract dislocation densities. The details of our in situ cantilever micro-beam bending experiment are outlined in section 3. In section 4 we characterize the bending induced deformation by applying the framework of section 2 and finally we discuss the results qualitatively and quantitatively in section 5, followed by an error discussion in section 6.

2. Geometrically necessary dislocations

2.1. Dislocation tensor

Nye introduced a tensor to describe a crystal's state of dislocation in terms of a local Burgers vector, [1]. This continuum based concept assumes a continuously dislocated state of the crystal lattice, which is mathematically described by a dislocation (or Nye) tensor field.[1] In principle, it allows the number of dislocations to increase to infinity, whereas their Burgers vectors may become infinitely small.

It is arbitrary with respect to which reference frame(s) this dislocation tensor is defined, but, as pointed out by Wheeler et al. [11], it is imperative to be consistent. In line with [27,28,11] we will use an enhanced summation convention, in which latin and greek subscripts stand for resp. the crystal[2] and the sample frame. Repeated indices are understood to be summed over the range $1, \ldots, 3$. For example, the tensor $\alpha_{i\gamma}$ describes the net Burgers vector content in a *crystal* direction x_i, from all dislocations that penetrate a unit area perpendicular to a chosen *sample* direction x_γ. Thus, all dislocations that penetrate an infinitesimal surface area perpendicular to a sample direction dl_γ yield a net Burgers vector db_i of

$$db_i = \alpha_{i\gamma}\, dl_\gamma. \tag{1}$$

The dislocation tensor is usually non-symmetrical and by that free of redundant information. Furthermore, its unit is L^{-1}, which means that a multiplication by a surface normal dl of unit L^2 delivers a Burgers vector with unit L^1.

The physical fact that individual dislocations neither end nor start within the crystal lattice is mathematically reflected in a conservation of the net Burgers vector. Within a closed circuit C, the net Burgers vector of all dislocations enclosed by the circuit is equal to that of all dislocations pointing through any surface S, limited by C, Fig. 1. That is, by integrating over surface S, we consider the total Burgers vector contribution of all dislocations enclosed by C,

$$b_i = \iint_S \alpha_{i\gamma}\, dS_\gamma. \tag{2}$$

By the introduction of a deformation tensor E, which locally relates the distorted lattice to the sample frame, an open Burgers
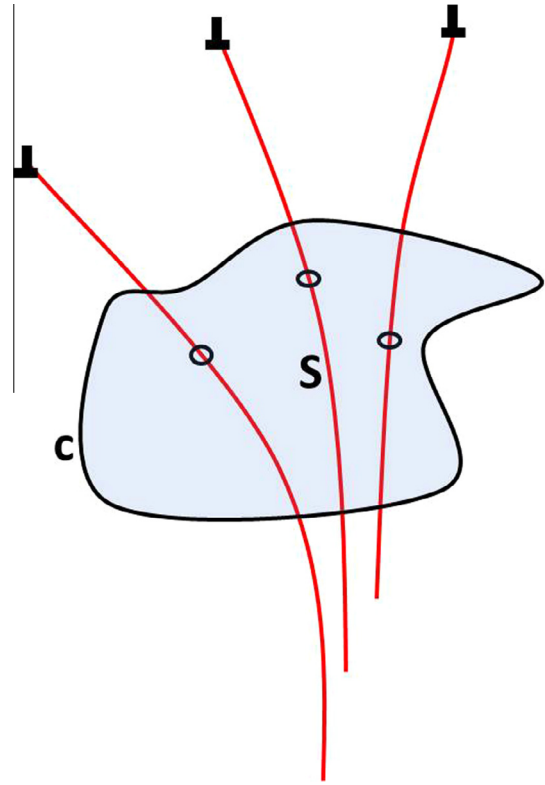
Fig. 1. Within a closed circuit C, the net Burgers vector of all dislocations enclosed by the circuit is equal to that of all dislocations pointing through any surface S, limited by C.

circuit along C' within the crystal frame can be converted to a closed circuit C within the sample frame, see Fig. 2:

$$b_i = -\int_{C'} \delta_{ij}\, dx_j = -\oint_C E_{i\gamma}\, dx_\gamma, \tag{3}$$

where δ_{ij} represents the identity tensor and a "−" sign is added to comply with the RHFS rule. By applying the Stokes theorem for 2nd order tensors, the line integral along C over E is converted to a surface integral of the curl of E over the enclosed surface S:

$$b_i = -\iint_S \nabla \times E_{i\gamma}\, dS_\gamma. \tag{4}$$

A direct comparison of Eqs. (2) and (4) then yields the fundamental equation of continuum dislocation theory:

$$\alpha_{i\gamma} = -\nabla \times E_{i\gamma} = -e_{\gamma\beta\alpha} E_{i\alpha,\beta}, \tag{5}$$

where e represents the Levi–Civita permutation tensor and $E_{i\alpha,\beta}$ represents a partial differentiation of the deformation tensor with respect to sample coordinates β.

The deformation E can be decomposed into a linear superposition of elastic lattice strain and lattice rotation (i.e. orientation). By assuming that GNDs tend to arrange in constellations of lowest energy (polygonization) the elastic strain contribution becomes negligible. Eq. (5) then simplifies to the curl of the orientation field:

$$\alpha_{i\gamma} = -\nabla \times g_{i\gamma} = -e_{\gamma\beta\alpha} g_{i\alpha,\beta}. \tag{6}$$

2.2. Reference frames

As emphasized by the subscripts, the dislocation tensor, α, in Eq. (6) is based on two reference frames that do not necessarily coincide. When the dislocation tensor is decomposed crystallographically into contributions of individual sets of dislocations this
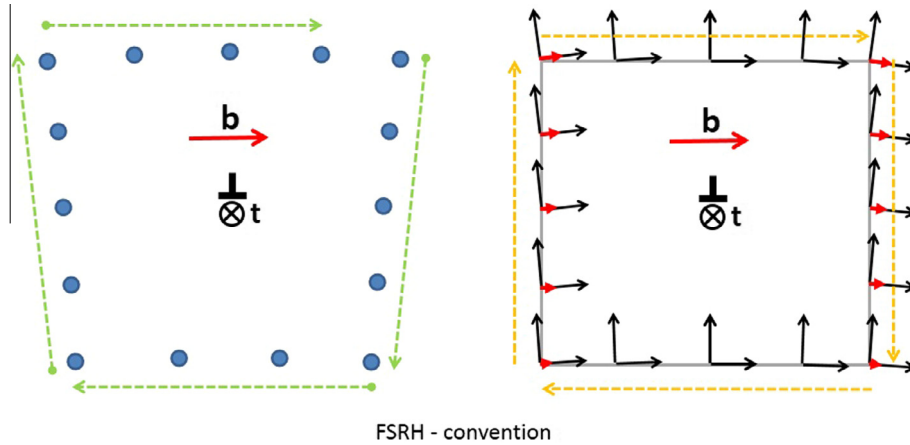
FSRH - convention

Fig. 2. Schematic of a Burgers circuit in a deformed crystal (left) and a sample frame (right). The tensor field to be integrated along the integration path is indicated by small black coordinate frames on the right. Only within the sample frame the integration path becomes closed, but still yields the same net Burgers vector as indicated by small red vectors.

has to be taken into account (Section 2.3). As pointed out by Wheeler et al. [11], it is perfectly possible to transform the dislocation tensor to a different set of reference frames by a pre- and/or post- multiplication with the (inverse) local orientation tensor, see Table 1. Independently, the differentiation inside the curl remains with respect to the chosen sample frame. Although all variant descriptions in Table 1 are equivalent, the first description proved to be most efficient for our computational purposes (Section 2.5).

In literature a 5th variant of Eq. (6) is often used, by an implicit change of the sample reference frame [3,8,9]. Consider two infinitesimally misaligned orientations g_1 and g_2. By a change of the sample reference frame to g_1 (i.e. $g_1 = I$), the infinitesimal lattice rotation between both orientations $d\omega = g_1 dg^T$ (Appendix A) simplifies with the help of Eq. (A.2) (in component notation) to

$$d\omega_{ij} = -dg_{i\gamma}. \tag{7}$$

Formally Eq. (7) appears contradictory, as both sides refer to different frames. However, by setting the sample reference frame identical to the local crystal frame, latin and greek subscripts refer to the very same frame. With this, Eq. (6) can now be expressed as

$$\alpha_{ij} = \nabla \times \omega_{ij} = e_{jkl}\,\omega_{il,k}. \tag{8}$$

Since both frames are identical, all previous four variants of Eq. (6) merge into Eq. (8). In being identical to the local crystal frame, the new sample frame now varies with the orientation field. This imposes a subtle but important constraint on the applicability of Eq. (8) to discrete orientation maps. Since they are acquired along a fixed discrete regular grid, differentiation along an arbitrary sample direction would require an interpolation of the orientation field.

2.3. Decomposition of the dislocation tensor

It was Nye [1] who pointed out that an arbitrary dislocation state can be constructed from a set of $K = 9$ linear independent dislocations, each weighted by an individual dislocation density, ρ:

$$\alpha_{ij} = \rho^k b_i^k \otimes t_j^k = \rho^k A_{ij}^k, \tag{9}$$

with $k = 1, 2, \ldots, K$ for each dislocation involved and b, t and A respectively for the Burgers vector, line element ($|t| = 1$) and dislocation dyadic and $\otimes$ to emphasize the otherwise implicit dyadic vector product.

In general, a dislocation dyadic consists of 3 screw components on the diagonal and 6 off-diagonal edge components. Depending

Table 1
Dislocation tensor for different reference frames.

Frames		Dislocation tensor
Crystal	Crystal	$\alpha_{ij} = -(\nabla \times g_{i\gamma})g_{\gamma j}$
Sample	Crystal	$\alpha_{\alpha j} = -g_{\alpha i}(\nabla \times g_{i\gamma})g_{\gamma j}$
Crystal	Sample	$\alpha_{i\gamma} = -(\nabla \times g_{i\gamma})$
Sample	Sample	$\alpha_{\alpha\gamma} = -g_{\alpha i}(\nabla \times g_{i\gamma})$

on the choice of the reference frame, the character of a dislocation can be inferred from its dyadic components. For pure edge and screw dislocations minimally one coefficient and for mixed dislocations minimally two coefficients will be non-zero. When deconstructing a dislocation tensor, it is imperative to keep the reference frames for Burgers vector and line element in line with those of the dislocation tensor as derived from Eq. (6). The line element represents a unitless direction of magnitude one, L^0. Thus, unit wise the product of dislocation density and Burgers vector matches with the dislocation tensor L^{-1}.

The only repeated index in Eq. (9) is the dislocation index, such that it expands as follows,

$$\begin{bmatrix} A_{11}^{k=1} & A_{11}^{k=2} & \cdots & A_{11}^{k=9} \\ A_{12}^{k=1} & A_{12}^{k=2} & \cdots & A_{12}^{k=9} \\ \vdots & \vdots & & \vdots \\ A_{33}^{k=1} & A_{33}^{k=2} & \cdots & A_{33}^{k=9} \end{bmatrix} \begin{bmatrix} \rho^{k=1} \\ \rho^{k=2} \\ \vdots \\ \rho^{k=9} \end{bmatrix} = \begin{bmatrix} \alpha_{11} \\ \alpha_{12} \\ \vdots \\ \alpha_{33} \end{bmatrix}. \tag{10}$$

Hence, a given dislocation tensor can be deconstructed into a set of linear independent dislocations and corresponding densities by essentially solving the inverse of a 9×9 compound dyadic matrix. The null space (i.e. $\alpha = 0$) of the compound dyadic in Eq. (10) represents all combinations of dislocation densities that remain without geometric impact. By definition they must represent SSD densities [29].

2.3.1. Crystallographic decomposition of the dislocation tensor

Although a crystallographic deconstruction is computationally more costly, it potentially enables a deeper insight into the underlying deformation mechanisms. In order to solve any dislocation densities, a set of dislocations must first be defined. An interpretation of the dislocation densities is served best with a set, chosen such that it reflects the slip systems of the material in question. Except for the simple cubic case (Section 2.3.2), the effective set

size, S, of a dislocation set after symmetrization, exceeds the maximum solvable number of $K = 9$ and leaves Eq. (10) in principle under-determined.

Essentially two methods are commonly employed to come to a solution within an S-dimensional dislocation density space [30,29,5,6,10,16,31,12]. An L^2 minimized S-dimensional density solution exists, which is explicitly solvable via a singular value decomposition of the compound dyadic. Alternatively, an L^1 minimized solution is computationally more costly (e.g. via a simplex heuristic) and can be based on the dislocation length, associated line energy or Schmid factor.

It is the components of the solution vector that represent GND densities. Thus, from a physical standpoint, a minimization of the sum of the absolute solution vector components (L^1-norm) is preferential over a minimization of the total solution vector length (L^2-norm).

Our approach is an L^1 minimization, in line with [10], with the difference that we minimized the associated line energy. The total number of combinations out of which a minimum yielding combination must be obtained, amounts for a subset of $K = 9$ dislocations out of a set size S to:

$$C_S^{K=9} = \binom{S}{9}, \quad (S \geqslant 9). \tag{11}$$

In Table 2 the theoretical number of combinations is listed for some common slip systems. It should be noted, though, that the number of linear independent combinations is usually lower. Furthermore, the uniqueness of the solution is not guaranteed.

2.3.2. Simple cubic decomposition of the dislocation tensor

In some cases it is sufficient to disregard the individual contributions in a dislocation set in favor of a total bulk density result. As pointed out by El-Dasher et al. and Ruggles et al. [6,12], it is defensible to avoid solving Eq. (9) altogether in order to come to a reasonable estimation. For this the dislocation tensor is deconstructed as in a simple cubic case, as introduced by Nye. With all line elements and Burgers vectors parallel to the reference frame axes, each dislocation dyadic comprises exactly one non-zero component. Due to this, the compound dyadic in Eq. (10) becomes sparse, with only non-zero elements on the diagonal,

$$\begin{bmatrix} A_{11}^{k=1} & 0 & \cdots & 0 \\ 0 & A_{12}^{k=2} & \cdots & 0 \\ \vdots & \vdots & & \vdots \\ 0 & 0 & \cdots & A_{33}^{k=9} \end{bmatrix} \begin{bmatrix} \rho^{k=1} \\ \rho^{k=2} \\ \vdots \\ \rho^{k=9} \end{bmatrix} = \begin{bmatrix} \alpha_{11} \\ \alpha_{12} \\ \vdots \\ \alpha_{33} \end{bmatrix}. \tag{12}$$

In consequence, the total bulk density, ρ_{tot}, can be conveniently expressed in terms of the entrywise 1-norm of the dislocation tensor, [6,12]:

$$\rho_{\text{tot}} = \sum_k |\rho^k| = \frac{1}{|b|} \sum_i \sum_j |\alpha_{ij}| = \frac{\|\alpha_{ij}\|_1}{|b|}. \tag{13}$$

Important constraints to this approximation are that it neither allows for multiple Burgers vector magnitudes nor is the total density outcome independent of the choice of reference frame. Effectively, it is thus limited to cubic symmetries and the term lower bound may seem not entirely apt. In spite of these limitations, the simple cubic deconstruction enables additional alternatives to quantify the dislocation content.

2.4. GND estimation based on the average disorientation angle

Physically, the dislocation density can be interpreted in terms of a low angle grain boundary model. For this, it is assumed that the

Lattice	Dislocations	Set size	Comb.
bcc	$b = \langle \frac{1}{2}\frac{1}{2}\frac{1}{2} \rangle, t = \frac{\sqrt{6}}{6}\langle 112 \rangle$ $b = \langle \frac{1}{2}\frac{1}{2}\frac{1}{2} \rangle, t = \frac{\sqrt{3}}{3}\langle 111 \rangle$	16	11440
fcc	$b = \langle \frac{1}{2}\frac{1}{2}0 \rangle, t = \frac{\sqrt{6}}{6}\langle 112 \rangle$ $b = \langle \frac{1}{2}\frac{1}{2}0 \rangle, t = \frac{\sqrt{2}}{2}\langle 110 \rangle$	18	48620
hex	$b = \langle a \rangle$, screw $b = \langle a \rangle$, basal edge $b = \langle a \rangle$, prism edge $b = \langle c + a \rangle$, pyr. screw $b = \langle c + a \rangle$, pyr. edge	21	293930

average misorientation, θ_{av}, of a pivot voxel with its surrounding voxels is accommodated by a simple low angle tilt grain boundary. This boundary type accommodates a lattice misorientation with a minimal number of dislocations. It may consist of a single set of parallel edge dislocations with a reciprocal distance of $1/d = \theta_{\text{av}}/|b|$, with b for the Burgers vector.

In a first approximation, the grain boundary is assumed to be located midway between the pivot voxel and its surrounding voxels and constructed of six cube faces, as indicated in Fig. 3. By assuming an equal step size of a in all dimensions, the total dislocation length per boundary fragment amounts to: $L = a^2 \theta_{\text{av}}/|b|$. As each boundary fragment connects two adjoining voxels, half of this length can be attributed to each voxel. The local dislocation density then results from relating the total dislocation length of all six boundary fragments to the pivot voxel volume:

$$\rho_{tot} = \frac{6}{2} \frac{\theta_{\text{av}} a^2}{|b|} \frac{1}{a^3} = \frac{3\theta_{\text{av}}}{|b| a}. \tag{14}$$

This and a similar result can also be derived in a more formal way, as shown in Appendix B.

2.5. Some computational considerations

In the following we address some computational issues that need to be taken care of when solving dislocation densities.

2.5.1. Choice of reference frames

Although all variants of Eq. (6) are equivalent, the first in Table 1 proves to be most efficient for an L^1 minimization. Only here α is independent of the sample reference frame and consequently the dislocation dyadics associated with it as well. The advantage is that all linear independent combinations of dislocation dyadics can be efficiently re-used at each data point. Although this is not very time-consuming in itself, the overall computation time quickly increases with the number of data points.

2.5.2. Symmetry

Although Eq. (6) will be applied to neighboring orientations that differ only slightly, the crystal symmetry of the orientation field must still be taken into account to ensure that the smallest dg between neighboring orientations is used and to ensure a consistent orientation description throughout the entire field.

A differential orientation between two neighboring orientations is described by $dg = g_2 - g_1$. In contrast to Δg, dg is not orthonormal and in consequence symmetry operators are not applicable. A minimal dg can be extracted via the corresponding disorientation $\Delta g_{\text{dis}} = g_1 g_2^{-1}$ from:

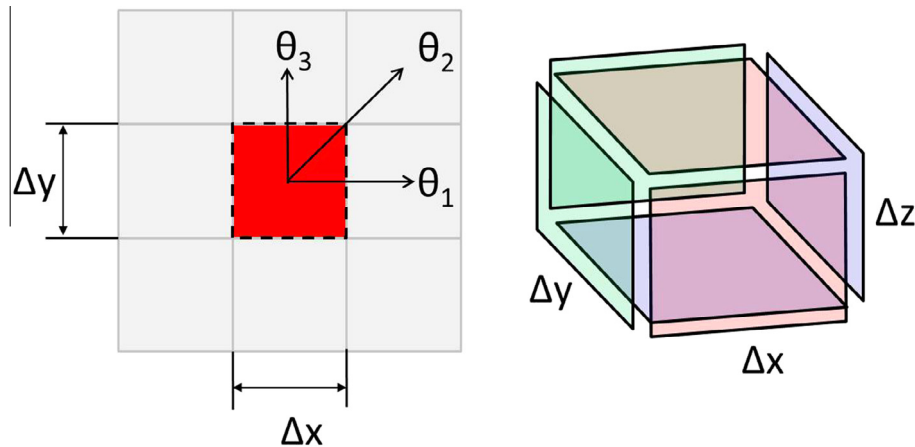$$dg = (\Delta g_{\text{dis}}^T - I)g_1. \tag{15}$$

Fig. 3. GND estimation based on the local average disorientation of a pivot voxel (red) with its first shell of neighbors (gray). The assumed low angle tilt GB is indicated by a dashed line (left) and shown in 3D (right) composed of 6 individual fragments. (For interpretation of the references to colour in this figure legend, the reader is referred to the web version of this article.)

By the choice of a specific symmetry operator for g, the crystal frame in $\alpha_{i\gamma}$ becomes tacitly specified and with that the outcome for $\alpha_{i\gamma}$ as well. Hence, when the curl is calculated the symmetry operator for a pivot orientation must be maintained constant in all three dimensions. Moreover, this specific symmetry operator must also be applied when transforming the corresponding $\alpha_{i\gamma}$ to another set of reference frames. From a computational point of view it is therefore advantageous to avoid any symmetrization of the pivot orientation, i.e. use it "as is". This imposes no additional constraint to Eq. (15) since it is always possible to find one arbitrary disorientation (and its inverse) by a symmetrization of just one of both orientations.

3. Experimental method

An in-plane cantilever micro-beam of about 21 μm × 3 μm × 3 μm was produced by Ga⁺-ion milling from an edge of a polycrystalline sample of pure and recrystallized copper in a Zeiss 1540 CrossBeam FEG SEM.

Before the milling process the sample was mechanically polished from two perpendicular surfaces to create a sharp edge. EBSD-based orientation mapping was performed on one of the sides in order to reveal the microstructure and crystal orientations. Subsequently, an area containing a large angle grain boundary was selected for the preparation of a cantilever micro-beam. In order to remove material that was possibly affected by surface strain, the two surfaces were first removed up to a depth of 3 μm, by Ga⁺-ion milling in grazing incidence along these surfaces. Next, the cantilever was prepared by milling with a Ga⁺-ion beam accelerated at 30 kV. For the removal of large volumes of material a 2 nA beam current was used, for fine finishing the beam current was reduced to 500 pA. Apart from the fixed end, the beam was completely cut free from the surrounding bulk material, see Fig. 4. The beam was cut such that it contained a single approximately cross-sectional grain boundary at about a third beam length distance from the fixed end.

The cantilever was deflected by positioning a micromanipulator tip (Kleindiek Nanotechnik) perpendicularly against its free end (end loaded cantilever beam). The force from the micromanipulator acted perpendicular only at the start of the experiment. With increasing beam deflection, the force angle decreased inevitably but had no noticeable influence on the deformation conditions of the cantilever. Limitations to the range of the micromanipulator

tip prevented a full deflection of the cantilever. Approximately 25% of the free end did not impact the anvil (see below) and remained virtually undeformed.

End loaded cantilever beams of this size deform differently compared to their macroscopic counterparts. Most of the imposed strain tends to accumulate around the fixed end, leading rather to buckling than to bending. In order to achieve a more homogeneous deformation state, the cantilever was deflected in a "mildly constrained" manner by milling a quarter-circle-shaped anvil below the actual cantilever, as is indicated in Fig. 4. This particular arrangement forced the cantilever to adopt a constant bending radius. Due to this constraint, a tangential point between the beam and the anvil existed, which gradually shifted from the fixed towards the free end with increasing deflection. This prevented already deformed volumes between the fixed end and the tangential point to take up further deformation. Through a constant activation of new slip systems alongside the shifting tangential point a more homogeneous deformation state was achieved, as compared to an unconstrained experiment.

After the cantilever had been deformed, a 3-dimensional orientation map of the beam was measured by 3D EBSD using a combination of serial sectioning with a Ga⁺-ion beam and EBSD orientation mapping on the individual sections [32]. Sectioning was performed with a 500 pA beam, milling for 2 min on a window of 300 nm thickness and a width as the cantilever length. This window was moved towards the milled surface by 100 nm for each serial section. The acquisition of EBSD data was done at 15 kV acceleration voltage using an EDAX-TSL Hikari detector at an acquisition rate of 100 Hz and 4 × 4 binning. A square acquisition grid with 100 nm step size was used. The patterns were analyzed with a Hough resolution of 120 pixels × 1° and a 9 × 9 convolution filter. The resulting dataset of 100 nm × 100 nm × 100 nm resolution was analyzed by an in-house developed 3D EBSD post processing software, QUBE.

4. Results

After acquisition of the 3D EBSD data set the slices were realigned (translational only) by minimizing the total inter-slice misorientation. The signal to noise ratio of the raw orientation data was improved by the application of a quaternion based median filter with a kernel size of 3 × 3 × 3 voxels and a cut-off angle of 4°. This noise-reducing and edge-preserving smoothing filter will be
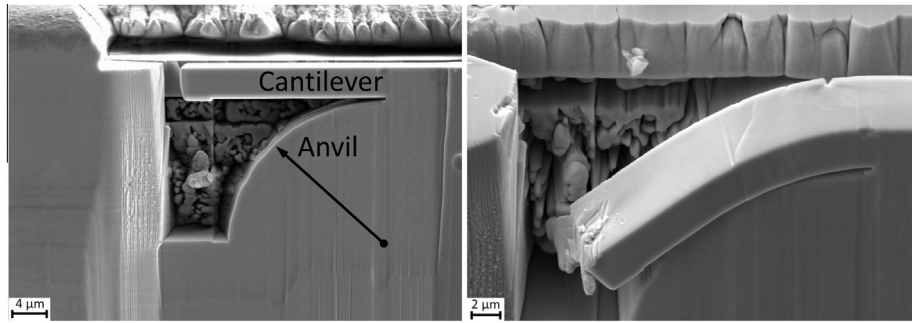
Fig. 4. SEM image of the cantilever micro-beam before (left) and after (right) bending. Observations at resp. 0° and 20° tilt.
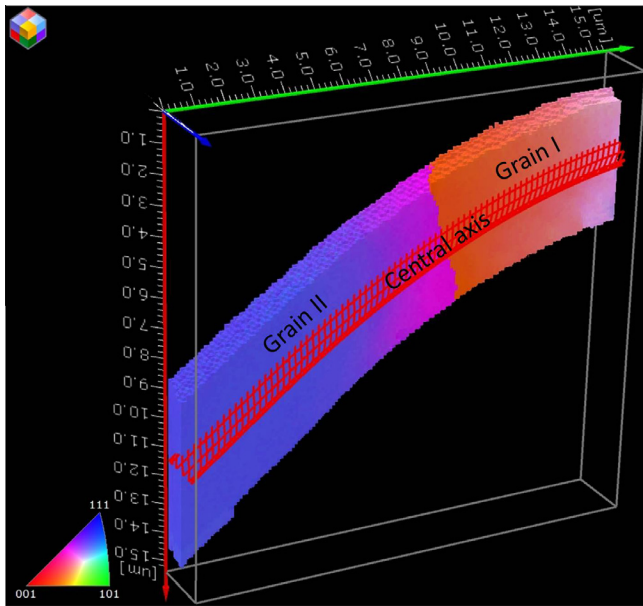

Fig. 5. Cross section of the cantilever micro-beam (unfiltered dataset). Color scheme: IPF-X, color indicates the crystallographic direction parallel to the sample frame x-axis (red). The central beam axis is indicated by a red wire tube of 500 nm radius. Its shape is based on a 2nd degree polynomial and linear fit to the external beam contours.
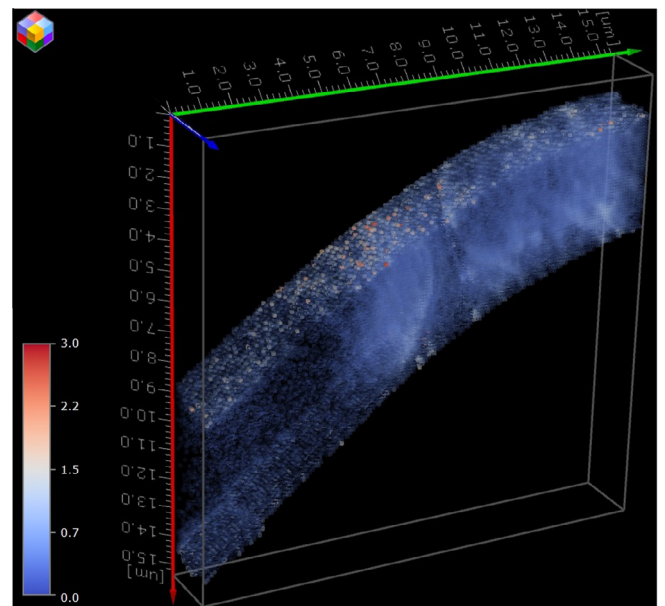

Fig. 6. Cantilever micro-beam (unfiltered dataset). Color scheme: local average disorientation (LAD) from 0° to 3°. Voxel opacity scales linearly with angle value.

outlined in a separate publication. Grains of similar orientation were then reconstructed with a critical threshold angle of 4°. This angle ensured a robust separation of the micro-beam from the anvil. In Fig. 5 a cross section of the bicrystalline beam is shown in an inverse pole figure color (IPF-X) scheme. Although slight color nuances tend to be obscured by the rendering technique, some overall orientation gradients in both grains can still be recognized.

The initial (undeformed) orientation of both grains is still preserved in the structure of the underlying quarter circle anvil (not shown). On average, both grains are misoriented by about 55.3°–⟨0.75,0.50,0.43⟩. For $\Sigma \leqslant 35$, no sufficiently close Coincidence Site Lattice (CSL) relation is found for this misorientation. Hence, it can be categorized as a random large angle grain boundary. After deformation, the misorientation in the vicinity of the grain boundary is confirmed to be nearly identical to that of their undeformed counterparts in the anvil.

In Fig. 6, the cantilever is represented in a local average disorientation (LAD) color scheme.[3] This color scheme encodes the

average disorientation angle of each voxel with its nearest neighbors (here 26), up to a chosen cut-off angle of 3°. Furthermore, the opacity of the voxels depends linearly on the LAD value. This representation allows an improved view into the volume by biasing larger values at the expense of smaller values.

Fig. 7 demonstrates the total summed GND density distribution as obtained according to section 2 on the unfiltered (a) as well as the median filtered (b) dataset. The opacity of the voxels scales with $\log \rho_{GND}$. The orientation curl was determined for directly neighboring voxels within a range of 0.0001° up to resp. 3° (unfiltered dataset) and 4° (median filtered dataset). The dislocation tensor was deconstructed into an FCC set of 12 pure edge and 6 pure screw dislocations. The L^1 minimization was based on the associated line energy, which is approximately 1.4 times higher for edge dislocations than for screw dislocations in copper. The total calculation time amounted to about 55 min on a Hewlet-Packard Z800 workstation with an Intel Xeon X5690 3.47 GHz processor.

The total GND density as shown in Fig. 7(b) can be conveniently split-up by the dislocation character. This is shown in Fig. 8 where the contributions from edge GNDs (a) and screw GNDs (b) are shown separately. Also here the voxel opacity scales with $\log \rho_{GND}$

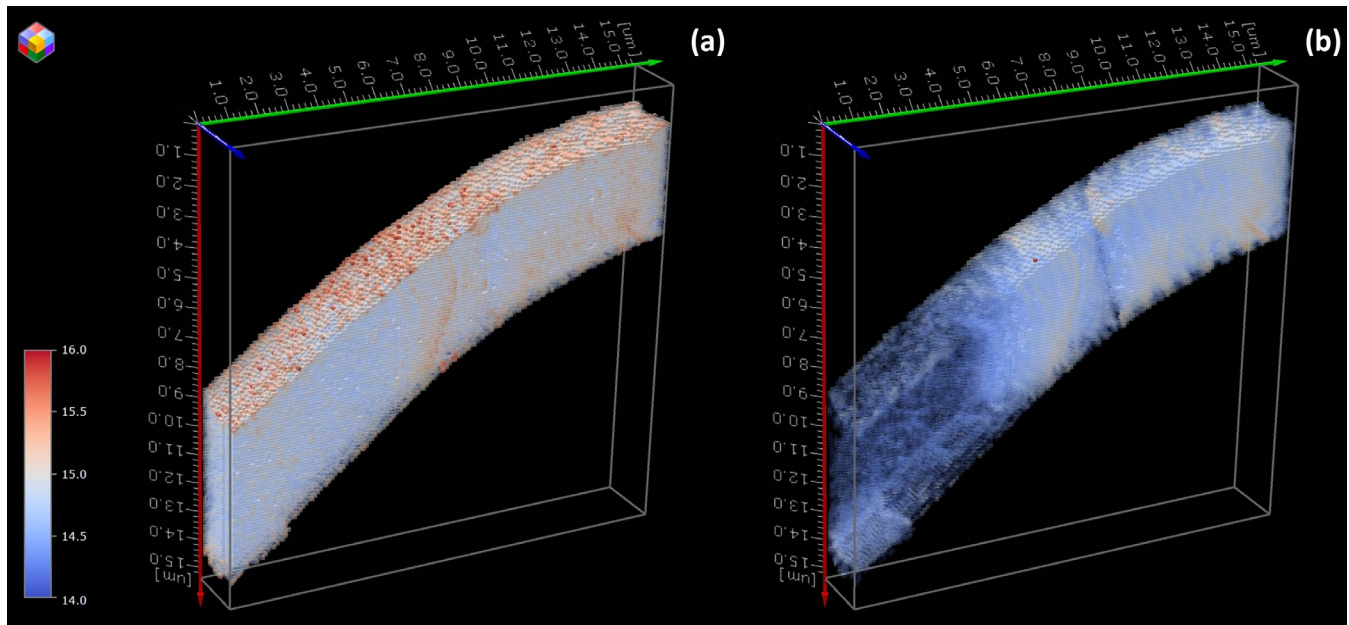[3] Comparable to "kernel average misorientation" or "local misorientation".

Fig. 7. Cantilever micro-beam. Color scheme: total GND density in the range from 1.0×10^{14} m^{-2} to 1.0×10^{16} m^{-2}. (a) Unfiltered dataset, GND cut-off angle 3°. (b) Median filtered dataset (kernel size: $3 \times 3 \times 3$, cut-off angle 4°), GND cut-off angle 4°. Voxel opacity scales with $\log \rho_{GND}$.
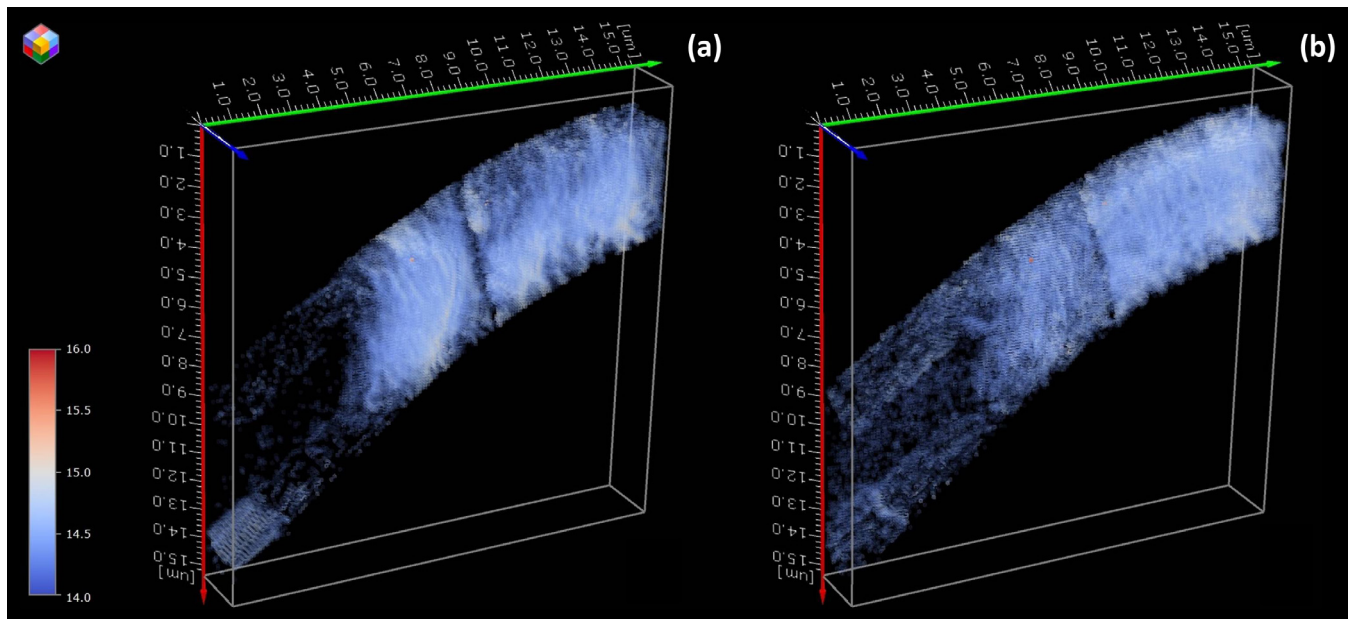

Fig. 8. Cantilever micro-beam, median filtered dataset (kernel size: $3 \times 3 \times 3$, cut-off angle 4°). Color scheme: (a) GND edge density (b) GND screw density in the range from 1.0×10^{11} m^{-2} to 1.0×10^{16} m^{-2}. Voxel opacity scales with $\log \rho_{GND}$.

5. Discussion

5.1. Bending vs. shearing

In order to use the present cantilever bending experiment for an assessment of the GND analysis method suggested here, it is relevant by which mechanism the deformation took place. During the bending process the beam may microscopically comply with the macroscopic shape change in two different manners or a mixture of them, as illustrated in Fig. 9. Either bending occurs by building-in GNDs and the associated lattice rotation (Fig. 9a), shortly *bending* in the following or it proceeds by a transition of

mobile dislocations on subsequent lattice planes without storage of any dislocations (Fig. 9b), shortly *shearing* in the following. If the deformation is carried mainly by the bending mechanism the GND density will be much higher than in the case of the shearing mechanism, in which a large number of dislocations will glide into the free surface.

Therefore, we calculated the average orientation along the central (or neutral) axis as is indicated in Fig. 5. The central axis has been approximated by a 2nd degree polynomial and a linear fit to the beam's external contours. The average orientation was based on all voxels within a radius of 500 nm around the central axis (red wire tube). The grain boundary intersects the central axis within a
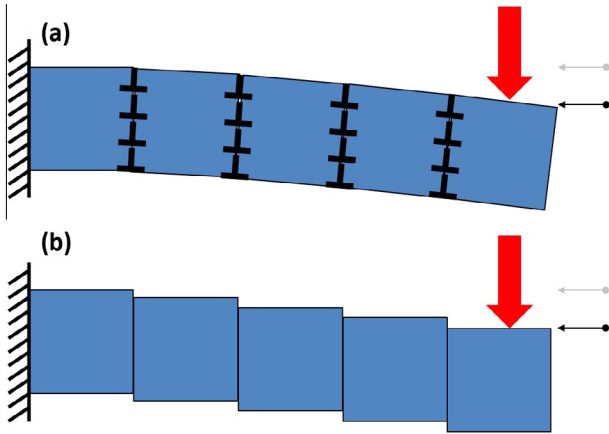
Fig. 9. Schematic of both limiting cases for the deformation of a cantilever microbeam. (a) Lattice rotation and storage of GNDs ("bending"). (b) Deformation without dislocation storage ("shearing").

small range (marked "GB" in Fig. 10) instead of a well-defined point because of a slight inclination.

As a reference for the original, undeformed beam orientation we picked two representative orientations from within the anvil. The average disorientation angle between the orientations on the central axis and the reference orientations was determined and compared to the macroscopic rotation of the cantilever, as described by the central axis, see Fig. 10.

It shows that the crystal rotation and the macroscopic rotation correspond closely. Any positive difference between the beam and lattice rotation (i.e., the lattice rotates less than the beam) is a suitable indication for the amount of additional shear that took place, cf. Fig. 10. The shape change of grain I is therefore largely supported by lattice rotation. Only close to the fixed end some additional shear can be noticed. A negative difference, as in grain II, implies a stronger lattice rotation (up to 3.5°) than the external beam shape change would demand.

From this we conclude that most of the deformation occurred mainly by the bending mechanism and that a contribution from the shearing mechanism has been largely negligible.

5.2. GND distribution

It can be seen from Fig. 6 that the part of the cantilever that has undergone deformation shows a dense network of steep orientation gradients throughout the volume. In contrast to that, the remaining part at the free end seems not to be affected very much.

The orientation gradient network is also reflected by a similar GND distribution, cf. Fig. 7. The GND image provides a more quantitative insight into the local deformation pattern though. In grain I, high GND densities are reached near the grain boundary and close to the free surface that touches the anvil. Compared to grain II the density distribution appears slightly more homogeneous. Not surprisingly, as both the GND and the LAD distributions depend on the misorientation, the overall tendency of the GND density distribution resembles the LAD distribution. However, due to the inherent averaging character of the LAD calculation, the qualitative resemblance with the GND distribution after median filtering is strongest, see Fig. 7(b).

The volume GND distribution is summarized by the (averaged) GND density profile along the central axis, see Fig. 11. Around the grain boundary a small volume of lower density levels is found, which sets in several voxels before the grain boundary. Therefore, the minimum seems genuine even though we did not compute a GND density across the grain boundary. This observation could possibly be understood as a consequence of local

hardening due to dislocation pile-ups at the boundary. This prevents further slip systems from being activated or to enter this volume which leads to a relative depletion of this volume. Another possibility could be a local change of the stress field due to the necessary strain accommodation across the boundary. This could prevent dislocations from the main deformation field to enter a volume in the vicinity of the boundary. Clearly, this result is opposite to recent findings by Jiang et al. [18], who found an increased GND density at the grain boundaries in polycrystalline copper. However, we attribute this contrast to a much smaller length scale in the present work.

Also shown in Fig. 11 is the (averaged) LAD profile along the central axis (blue). The GND and the LAD profiles show a strong resemblance. An approximation of the GND density (red), based on Eq. (14), shows indeed a very close match for grain I but also an overshoot for grain II. Apparently, the assumptions for Eq. (14) (Appendix B) are less valid for grain II than for grain I.

A comparison of the contributions from edge and screw GNDs, Fig. 8, reveals a different character of their respective distributions. Edge dislocations can be associated with the observed density hot spots, while screw dislocations are more homogeneously distributed. This difference is also confirmed by the (averaged) profile along the central axis, cf. Fig. 12. The screw GND density profile is less pronounced, compared to the edge GND density profile. Also, their relative contribution to the total GND density differs dramatically between both grains. In grain II, the edge contribution is more than twice as high as the screw contribution. Possibly, this difference originates from an activation of different slip systems due to a different grain orientation. Furthermore, considering the fact that edge dislocations generate a stronger lattice rotation than screw dislocations,[4] this could explain the observed local peak in the lattice rotation, Fig. 10.

5.3. Assessment of GND density levels

As a lower bound estimation of the expected GND density we assume that the lattice curvature is facilitated by radially aligned sets of low angle tilt grain boundaries, as shown in Fig. 9(a). Furthermore, we will assume the cantilever to be single crystalline with a suitable orientation such that the macroscopic shape change is possible with a minimum dislocation density (lower bound).

The homogeneous dislocation density ρ that arises from a simple low angle tilt grain boundary of misorientation θ and (effective) width Δx is given by:

$$\rho = \frac{\theta}{|b| \Delta x}. \tag{16}$$

In a most homogeneous case, all low angle tilt grain boundaries are assumed to be equidistant at Δx, all along the length l of the beam. This means that the total bending angle of the beam θ_{tot} is dispersed over $l/\Delta x$ boundaries (polygonization). The misorientation angle per boundary will then amount to $\theta = \theta_{tot} \Delta x/l$. Substitution into Eq. (16) delivers the following dislocation density:

$$\rho_{hom} = \frac{\theta_{tot}}{|b| l}. \tag{17}$$

In contrast, in a case of strongest possible localization, just one grain boundary accommodates the total bending angle of the beam. The local dislocation density becomes:

$$\rho_{inhom} = \frac{\theta_{tot}}{|b| \Delta x}. \tag{18}$$

---

[4] A low angle twist grain boundary needs a twice as high dislocation density as a tilt grain boundary of identical misorientation.
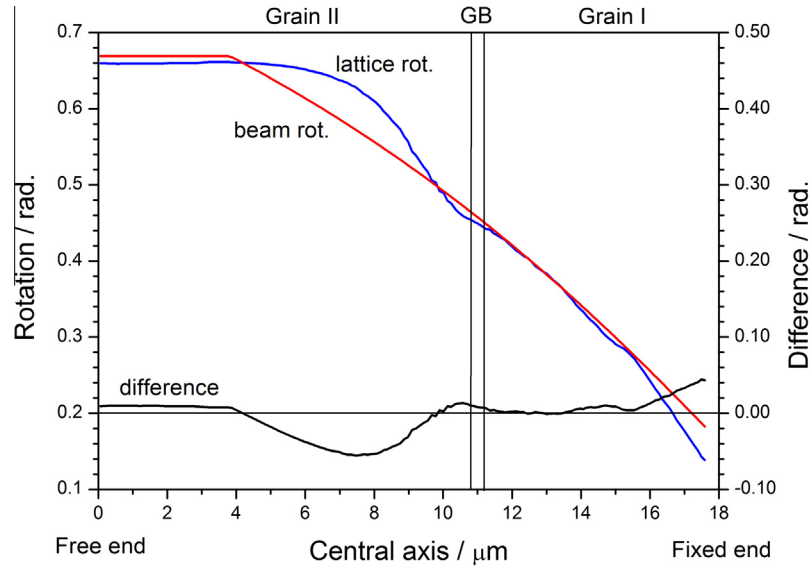
Fig. 10. Profiles of crystal (blue) and beam (red) rotation along the central beam axis, as indicated in Fig. 5. The crystal rotation is determined with respect to its original orientation. The difference between both rotations is shown in black. The position of the grain boundary is marked by "GB". (For interpretation of the references to colour in this figure legend, the reader is referred to the web version of this article.)
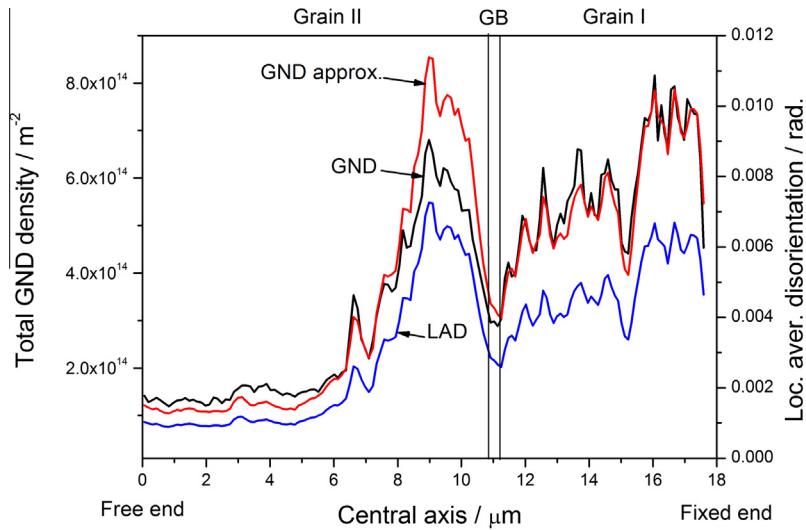

Fig. 11. Profiles of the total GND density (black) and the local average disorientation (LAD) angle (blue) along the central beam axis, as indicated in Fig. 5. The LAD based GND approximation from Eq. (14) is shown in red. The position of the grain boundary is marked by "GB". (For interpretation of the references to colour in this figure legend, the reader is referred to the web version of this article.)

The ratio of both cases, $\rho_{\text{inhom}}/\rho_{\text{hom}} = l/\triangle x$ demonstrates that, depending on the degree of localization strong fluctuations in the dislocation density can be expected. If averaged over the total beam length, both estimations will become identical, though, which illustrates that for a comparison the average density will be most suitable.

With a bending radius $R = l/\theta_{\text{tot}} = 16.25\,\mu\text{m}$ and a Burgers vector of $|b| = 2.55\,\text{Å}$ Eq. (17) delivers a GND density of $\rho_{\text{hom}} = 2.4 \times 10^{14}\,\text{m}^{-2}$. This estimate is in good agreement with the experimentally obtained average dislocation density for grain I of $3.5 \times 10^{14}\,\text{m}^{-2}$ (median filtered dataset). The partial deformation of grain II resulted in a slightly lower average dislocation density of $1.3 \times 10^{14}\,\text{m}^{-2}$ (median filtered dataset). For the unfiltered dataset, the experimental values are somewhat higher, grain I: $1.2 \times 10^{15}\,\text{m}^{-2}$ and grain II: $8.6 \times 10^{14}\,\text{m}^{-2}$. Clearly, this can be attributed to a stronger orientation noise in the unfiltered dataset.

6. Error analysis

In the following, we evaluate the impact of several error sources on the GND density. We disregard systematic errors that arise from the EBSD system, such as the calibration or the band detection algorithm. From an inspection of Eq. (6) it follows that the main errors are relative orientational and positional inaccuracies. We start, however, with the validity of Eq. (6).

6.1. Differentiability

The validity of the right hand side in Eqs. (6) and (8) depends directly on the differentiability of the orientation tensor field. As shown in Appendix A, the expression for a differential orientation $dg = g_2 - g_1$ represents a lattice rotation, only to the amount to which the term $\eta = dg\,dg^T$ remains negligible.
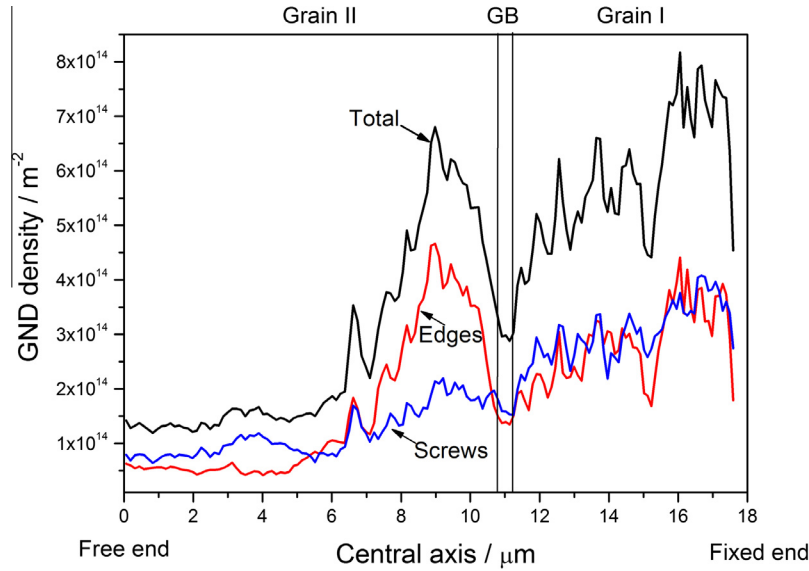
Fig. 12. Profile of the total GND density (black) as well as contributions from screw GNDs only (blue) and edge GNDs only (red) along the central beam axis, as indicated in Fig. 5. The position of the grain boundary is marked by "GB". (For interpretation of the references to colour in this figure legend, the reader is referred to the web version of this article.)

This rather abstract error can be quantified for the case of a low angle tilt grain boundary. Suppose both reference frames on either side of the boundary are tilted around a common x-axis by an angle θ and the boundary plane is perpendicular to e.g. the y-axis. The difference in orientation, dg, between both frames is then given by:

$$dg = \begin{bmatrix} 0 & 0 & 0 \\ 0 & cos\theta - 1 & -sin\theta \\ 0 & sin\theta & cos\theta - 1 \end{bmatrix} \simeq \begin{bmatrix} 0 & 0 & 0 \\ 0 & 0 & -sin\theta \\ 0 & sin\theta & 0 \end{bmatrix}. \quad (19)$$

The latter matrix represents a true rotation, whereas the first matrix strictly only does for $\theta \to 0$. For sake of simplicity, we assume no misorientation in x and z, through which the corresponding dislocation tensors become as follows:

$$\alpha = \frac{1}{\Delta y} \begin{bmatrix} 0 & 0 & 0 \\ -sin\theta & 0 & 0 \\ cos\theta - 1 & 0 & 0 \end{bmatrix} \simeq \frac{1}{\Delta y} \begin{bmatrix} 0 & 0 & 0 \\ -sin\theta & 0 & 0 \\ 0 & 0 & 0 \end{bmatrix}. \quad (20)$$

Without any assumption about the dislocation type the lower bound approximations already reveal an overall dislocation density of resp. $\rho_1 = \frac{|sin\theta| + |cos\theta - 1|}{|b|\Delta y}$ and $\rho_2 = \frac{|sin\theta|}{|b|\Delta y}$. While ρ_2 is in accordance with theory, ρ_1 is too high by a factor $cos\theta - 1$, Fig. 13. For small θ, this error can be approximated by a Taylor polynomial, $\propto \frac{1}{2}\theta^2$. As a quantification, Fig. 13 also shows the relative error in dislocation density, $(\rho_1 - \rho_2)/\rho_2$. For this particular example it reaches up to 13% at an angle of 15°. It can be anticipated, though, that this error will be different for more complex dislocation tensors.

In general, we can conclude that with an increasing disorientation angle the GND density is increasingly overestimated. As a consequence, disorientations above a certain angle need to be excluded.

6.2. Positional errors

Any discrepancy between the assumed and the actual probing position of the electron beam represents a positional error. Main sources for in-plane positional errors are a deflection of the electron beam, a position change of the sample and sample tilt, [33,32].

The first two are generally addressed as "drift" and are due to, for example, capacitive charging effects or mechanical variations of the stage. As drift tends to increase piecewise with time, two measurement points experience a drift difference that increases with the time span between their acquisition. Hence, neighbouring points in an individual scan line tend to have the smallest relative drift, while neighbouring points in different serial sections of a 3D data set may show the largest relative drift. As a consequence, drift predominantly appears as a mismatch between neighbouring slices. It can be corrected for, to some extent, by a minimization of the mismatch between two sections (slice re-alignment), [32]. The success of this procedure is, however, limited by the in-slice drift. This drift is usually much less systematic in character and therefore more difficult to correct for.

The error from misaligned slices can be roughly estimated with Eq. (14). If, on average, the misorientation angles between neighbouring voxels are equal, $|\theta_x| \simeq |\theta_y| \simeq |\theta_z|$, then a change of $|\theta_z|$ by a factor f will have an effect on the total density of:

$$\frac{\rho_{tot}^*}{\rho_{tot}} \simeq \frac{2 + f}{3}. \quad (21)$$

Hence, under these assumptions a 100% increase in θ_z will cause an increase of the GND density by 1/3.

Apart from in-plane errors, FIB milled surfaces can exhibit also out-of-plane errors, such as a non-parallelity of neighbouring slices or surface roughness (curtaining). These errors are, however, usually smaller than the drift related ones.

6.3. Orientation errors

Under good conditions, literature estimates for the relative orientation error in Hough based EBSD range between 0.2° and 0.5° [34,13,17]. However, with increasing acquisition speed, compromises with regard to pattern and Hough-space resolution become necessary, all with the consequence of a higher relative and absolute error. Hence, due to a limited instrument time, 3D EBSD typically suffers from a higher orientation noise than 2D EBSD conducted under good conditions. Orientation noise translates into corresponding contributions to the GND density. This represents a random background to the true GND signal and is frequently
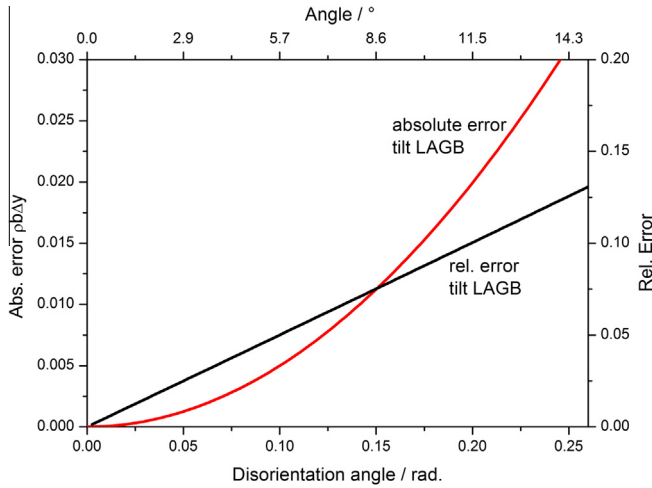
Fig. 13. Absolute (left axis) and relative (right axis) error for a tilt LAGB as a function of the disorientation angle.

addressed as spurious density. The spurious GND density that arises from a given misorientation noise can be approximated by Eq. (14). Apart from an additional factor of 3 this approximation is equivalent to an earlier approach by He et al. [8]:

$$\rho_{sp} = \frac{3\theta_n}{|b| a}, \qquad (22)$$

with ρ_{sp} for the spurious density, θ_n for the misorientation noise angle, b for the Burgers vector and a for the step size.

A GND density must be sufficiently high compared to the spurious density. This demand can be expressed in terms of a signal to noise ratio, snr, of the average GND density to the spurious density, $snr = (\rho/\rho_{sp})^2$. A substitution in Eq. (22) delivers

$$\rho = \frac{3\theta_n snr^{\frac{1}{2}}}{|b| a}. \qquad (23)$$

With this, it is possible to illustrate the effect of filtering on the spurious density in grain I. For the unfiltered dataset, a mean GND density of 1.2×10^{15} m^{-2} was obtained. Under the assumption of

Fig. 14. Lower and upper limits for the step size as proposed by Kysar et al. [31]. Burgers vector $b = 2.55$ Å. The combinations of step size and GND densities, as obtained for grain I, are indicated by "A" (unfiltered dataset) and "B" (median filtered dataset). An additional lower limit for the step size, as given by Eq. (24) is shown as an example for both data points. Point A: $snr = 8.5$ and $\theta_n = 0.2°$; point B: $snr = 8.5$ and $\theta_n = 0.06°$. (For interpretation of the references to colour in this figure legend, the reader is referred to the web version of this article.)

$\theta_n \approx 0.2°$, Eq. (23) yields a $snr \approx 8.5$. If, conservatively at least a similar snr is assumed for the median filtered dataset, then for a mean density of 3.5×10^{14} m^{-2} the misorientation noise at the same step size has been reduced to $\theta_n \leqslant 0.06°$.

6.4. Step size

It is evident from Eq. (6) that the dislocation density depends on the acquisition step size. Fundamental to our analysis is the assumption of a continuous dislocation density. In an approach by Kysar et al. [31] this imposes a lower limit to the acquisition step size of the average dislocation spacing, approximated by $1/\sqrt{\rho}$. Towards the higher end, they argued that the step size should be limited by the length scale of the main frequencies in the deformation field (e.g. the subgrain size), estimated by $1/\rho b$, Fig. 14. As pointed out by Jiang et al. [19], within the step size limits set above, the GND density that is resolved can still vary somewhat. In this context, it is important to note that the discrimination between GNDs and SSDs, afterwards by analytical means, is mainly a matter of step size and due to that not necessarily in line with a general physical understanding of GNDs and SSDs. For instance, at a step size too large two opposite GNDs would cancel each other out and remain undetected. Jiang et al. [19] observed this effect as a decrease of the GND density with increasing step size in strained copper.

Without claiming completeness we conclude that the step size of 1×10^{-7} m as used in the present work, complies with the step size limitations for the obtained average GND densities, ranging between 1.3×10^{14} m^{-2} and 1.2×10^{15} m^{-2}. In general the relative contribution from noise in a GND signal will also change with the step size. Orientation noise itself is independent of the step size by definition. If e.g. a linear orientation gradient (with a constant rotation axis) is sampled with a decreasing step size, it follows from Eq. (6) that the noise contribution in the GND signal is relatively increased. In order for the GND signal to be sufficiently larger than the spurious density, a step size must be integrative, i.e. large, enough [35]. Given a minimum signal to noise ratio, snr_{min}, it follows from Eq. (23) that the step size must exceed

$$a \geqslant \frac{3\theta_n snr_{min}^{\frac{1}{2}}}{|b| \rho}. \qquad (24)$$

This lower limit to the step size is characterized by the numerator in Eq. (24). As an example, it is shown in Fig. 14, for the snr and θ_n as obtained for grain I in section 6.3.

7. Conclusions

In the present paper we have reconsidered the existing theories for the calculation of GND densities from 3D orientation fields, as acquired for example by 3D EBSD. Importantly, we have highlighted the role of the reference frames in detail when calculating Nye's dislocation tensor. Furthermore, we have shown that, provided a number of assumptions are satisfied, the total GND density can be approximated quite accurately from the local average disorientation angle.

A second important point concerns the consideration of various error sources. In line with other authors, we identified orientation noise and misalignment due to drift as the most important errors for small misorientations. Furthermore, we discussed the differentiability of the orientation field, which decreases with increasing misorientation angle and a suitable range for the acquisition step size.
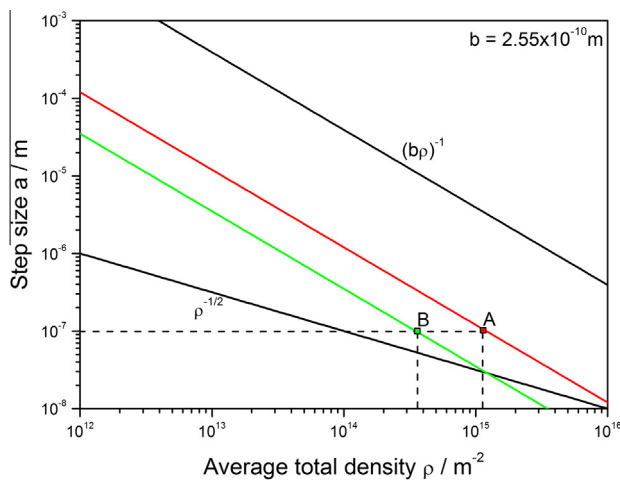
Our theoretical considerations are complemented by a well-controlled micro cantilever bending experiment on a copper bicrystal. Through a comparison of the macroscopic cantilever rotation with the internal crystal rotation it was shown that the cantilever deformed mainly by a bending mechanism and not by a shearing mechanism. Subsequently, we compared the experimentally determined GND densities from a 3D EBSD data set with a theoretical lower bound estimation for a homogeneous bending of a cantilever. The theoretically and experimentally determined values agree very well, which demonstrates that the experimental approach is suitable to validate our 3D GND calculations. Additionally, we made two observations: A distinct difference in the edge GND to screw GND density ratios between both grains, as well as a local minimum in the total GND density distribution at the grain boundary.

Appendix A. Infinitesimal misorientations

Suppose two orientations g_1 and g_2 which are both orthonormal but also sufficiently close, such that holds: $g_2 \approx g_1 + dg$. The orthonormality condition, $gg^T = I$, then unfolds for g_2 (in terms of g_1) as follows [36]:

$$g_1 g_1^T + g_1 dg^T + dg g_1^T + dg dg^T = I, \tag{A.1}$$

with I for the identity matrix. By neglecting the last term on the left hand side and by introducing a $d\omega = g_1 dg^T$ the previous equation can be written as:

$$d\omega + d\omega^T \approx 0. \tag{A.2}$$

Thus for sufficiently small misorientations, $d\omega$ represents a skew symmetric matrix. Due to a vanishing trace, $d\omega$ represents an infinitesimal rotation whose axis is specified by the off-diagonal components.

Appendix B. GND approximation

Suppose again two orientations, as in Appendix A, which are sufficiently close. If the sample frame is changed to one of both crystal frames, one orientation becomes the identity, δ_{ij}, whereas the other becomes the disorientation, Δg_{ij}, between both orientations. The orientation difference is then approximated by a skew symmetric matrix: $d\omega_{ij} = \Delta g_{ij} - \delta_{ij}$. The matrix $d\omega_{ij} = e_{ijk}\bar{\omega}_k$ comprises the elements of an infinitesimal rotation vector $\bar{\omega}_k$.

With the aid of the curvature tensor $\kappa_{ij} = \bar{\omega}_{i,j}$ Eq. (8) can be formulated as:

$$\alpha_{ij} = e_{jkl} e_{ilm} \kappa_{mk}. \tag{B.1}$$

which simplifies to Nye's relation between the dislocation tensor and the lattice curvature:

$$\alpha_{ij} = \kappa_{ji} - \delta_{ji}\kappa_{mm}. \tag{B.2}$$

Assumption 1. By discretizing the curvature with an average rotation angle,[5] θ_{av}, around a unit disorientation vector, r, and a constant step size, a, in all dimensions the previous equation can be expanded as follows

$$\alpha_{ij} \simeq \frac{\theta_{av}}{a} \begin{bmatrix} -r_{22} - r_{33} & r_{21} & r_{31} \\ r_{12} & -r_{11} - r_{33} & r_{32} \\ r_{13} & r_{23} & -r_{11} - r_{22} \end{bmatrix}, \tag{B.3}$$

---

[5] In a strict sense; the LAD of only face touching voxels, in a $2 \times 2 \times 2$ kernel.

in which r_{ij} stands for the ith component of the unit disorientation vector between two orientations, neighboring in the jth dimension.

Assumption 2. We limit the approximation to a single type of Burgers vector, i.e., for cubic crystal symmetries only. This allows it, by taking the entrywise 1-norm of Eq. (B.3), to come to an estimation of the total GND density.

Assumption 3. A further simplification is possible by omitting an evaluation of the disorientation axes altogether. This is possible for specific statistical distributions of the disorientation axes.

Random disorientation axes: In each row of Eq. (B.3) the sum of the absolute off-diagonal terms represents an "incomplete" L^1-norm of the unit disorientation vector r, e.g. in row 1: $| r_2 | + | r_3 |$. Such an "incomplete" L_1-norm will range between 0 and $\sqrt{2}$, with a numerically determined expectation value of ≈ 1. A similar argument holds for the diagonal elements; the numerically determined expectation value amounts $\approx \sqrt{2}/2$. With this, the entry-wise 1-norm of Eq. (B.3) can be approximated as:

$$\rho_{tot} \simeq \frac{3(2+\sqrt{2})\theta_{av}}{2a | b |} \simeq \frac{5\theta_{av}}{a | b |}. \tag{B.4}$$

If crystallographic symmetry effects are considered, disorientation axes are no longer evenly distributed and consequently a change to Eq. (B.4) should be anticipated. However, a numerical evaluation of crystallographically randomly distributed disorientation axes (Laue class: $m\bar{3}m$), for disorientations up to 15°, resulted in only minor changes to Eq. (B.4).

Textured disorientation axes: In a symmetrical low angle tilt grain boundary, the disorientation axis lies within the boundary plane. Hence, the physical low angle tilt grain boundary model introduced in section 2.4 represents a case with a strong texturing of the disorientation axes. It is then easy to see that in Eq. (B.3) all r_{ii} components must be naught and of the r_{ij} components only three are one, whereas the remaining ones must be naught as well. With this, the entry-wise 1-norm approximation delivers exactly the same result as Eq. (14):

$$\rho_{tot} \simeq \frac{3\theta_{av}}{a | b |}. \tag{B.5}$$

Both Eqs. (B.4) and (B.5) represent a coarse but efficient approximation of the overall GND density based on the local average disorientation. They can be regarded as an approximation for two extreme statistical distributions of the disorientation axes in Eq. (B.3). Given the assumptions, they also confirm the existence of an approximate scaling between the GND density and the average disorientation angle.

References

[1] J.F. Nye, Some geometrical relations in dislocated crystals, Acta Mater. 1 (1953) 153–162.
[2] E. Kröner, Der fundamentale Zusammenhang zwischen Versetzungsdichte und Spannungsfunktionen, Z. Phys. 142 (1955) 463–475.
[3] E. Kröner, Allgemeine Kontinuumstheorie der Versetzungen und Eigenspannungen, Arch. Rotation. Mech. Anal. (1959).
[4] B.A. Bilby, R. Bullough, E. Smith, Continuous distributions of dislocations: a new application of the methods of non-Riemannian geometry, Proc. R. Soc. Lond. 231 (1185) (1955) 263–273. Series A.
[5] S. Sun, B.L. Adams, W.E. King, Observation of lattice curvature near the interface of a deformed aluminium bicrystal, Phil. Mag. A 80 (1) (2000) 9–25.
[6] B.S. El-Dasher, B.L. Adams, A.D. Rollett, Viewpoint:experimental recovery of geometrically necessary dislocation density in polycrystals, Scr. Mater. 48 (2003) 141–145.
[7] D.P. Field, P.B. Trivedi, S.I. Wright, Analysis of local orientation gradients in deformed single crystals, Ultramicroscopy 103 (2005) 33–39.

[8] W. He, W. Ma, W. Pantleon, Microstructure of individual grains in cold-rolled aluminium from orientation inhomogeneities resolved by electron backscattering diffraction, Mat. Sci Eng. A Struct. 494 (2008) 21–27.

[9] W. Pantleon, Resolving the geometrically necessary dislocation content by conventional electron backscattering diffraction, Scr. Mater. 58 (2008) 994–997.

[10] E. Demir, D. Raabe, N. Zaafarani, S. Zaefferer, Investigation of the indentation size effect through the measurement of the geometrically necessary dislocations beneath small indents of different depths using EBSD tomography, Acta Mater. 57 (2009) 559–569.

[11] J. Wheeler, E. Mariani, S. Piazolo, D.J. Prior, P. Trimby, M.R. Drury, The weighted Burgers vector: a new quantity for constraining dislocation densities and types using electron backscatter diffraction on 2D sections through crystalline materials, J. Microscopy 233 (2009) 482–494. Pt. 3.

[12] T.J. Ruggles, D.T. Fullwood, Estimations of bulk geometrically necessary dislocation density using high resolution EBSD, Ultramicroscopy 133 (2013) 8–15.

[13] A.J. Wilkinson, G. Meaden, D.J. Dingley, Elastic strain tensor mapping – extending the limits of EBSD analysis, Microsc. Microanal. 11 (Suppl 2) (2005).

[14] T.B. Britton, A.J. Wilkinson, Measurement of residual elastic strain and lattice rotations with high resolution electron backscatter diffraction, Ultramicroscopy 111 (2011) 1395–1404.

[15] J. Kacher, C. Landon, B.L. Adams, D. Fullwood, Bragg's law diffraction simulations for electron backscatter diffraction analysis, Ultramicroscopy 109 (2009) 1148–1156.

[16] A.J. Wilkinson, D. Randman, Determination of elastic strain fields and geometrically necessary dislocation distributions near nanoindents using electron back scatter diffraction, Phil. Mag. 90 (2010) 1159–1177.

[17] C.J. Gardner, B.L. Adams, J. Basinger, D.T. Fullwood, EBSD-based continuum dislocation microscopy, Int. J. Plasticity 26 (2010) 1234–1247.

[18] J. Jiang, T.B. Britton, A.J. Wilkinson, Evolution of dislocation density distributions in copper during tensile deformation, Acta Mater. 61 (2013) 7227–7239.

[19] J. Jiang, T.B. Britton, A.J. Wilkinson, Measurement of geometrically necessary dislocation density with high resolution electron backscatter diffraction: Effects of detector binning and step size, Ultramicroscopy 125 (2013) 1–9.

[20] T.J. Hardin, B.L. Adams, D.T. Fullwood, R.H. Wagoner, E.R. Homer, Estimation of the full Nye's tensor and its gradients by micro-mechanical stereo-inference using EBSD dislocation microscopy, Int. J. Plasticity 50 (2013) 146–157.

[21] D. Field, Quantification of dislocation structure heterogeneity in deformed polycrystals by EBSD, Model. Simul. Mater. Sc. 20 (2012) 1–12.

[22] M.F. Ashby, The deformation of plastically non-homogeneous materials, Phil. Mag. 21 (170) (1970) 399–424.

[23] J.S. Stölken, A.G. Evans, A microbend test method for measuring the plasticity length scale, Acta Materialia 46 (14) (1998) 5109–5115.

[24] E. Demir, D. Raabe, F. Roters, The mechanical size effect as a mean-field breakdown phenomenon: Example of microscale single crystal beam bending, Acta Mater. 58 (5) (2010) 1876–1886.

[25] E. Demir, D. Raabe, F. Roters, Bending of single crystal microcantilever beams of cube orientation: Finite element model and experiments, J. Mech. Phys. Solids 58 (10) (2010) 1599–1612.

[26] E. Demir, D. Raabe, Mechanical and microstructural single-crystal Bauschinger effects: Observation of reversible plasticity in copper during bending, Acta Mater. 58 (18) (2010) 6055–6063.

[27] J.W. Christian, Transformations in Metals and Alloys Part 1: Equilibrium and General Kinetic Theory, Pergamon Press, 1975.

[28] A.P. Sutton, R.W. Balluffi, Interfaces in Crystalline Materials, Clarendon Press, 1995.

[29] A. Arsenlis, D.M. Parks, Crystallographic aspects of geometrically-necessary and statistically-stored dislocations, Acta Mater. 47 (5) (1999) 1597–1611.

[30] B.L. Adams, Orientation imaging microscopy: emerging and future applications, Ultramicroscopy 67 (1997) 11–17.

[31] J.W. Kysar, Y. Saito, M.S. Oztop, D. Lee, W.T. Huh, Experimental lower bounds on geometrically necessary dislocation density, Int. J. Plasticity 26 (2010) 1097–1123.

[32] S. Zaefferer, S. Wright, D. Raabe, 3D-orientation microscopy in a FIB SEM: A new dimension of microstructure characterisation, Microsc Microanal. 13 (Suppl 2) (2007) 1508–1509.

[33] G. Nolze, Image distortions in SEM and their influences on EBSD measurements, Ultramicroscopy 107 (2–3) (2007) 172–183.

[34] S.I. Wright, J.A. Basinger, M.M. Nowell, Angular precision of automated electron backscatter diffraction measurements, Mater. Sci. Forum 702–703 (2012) 548–553.

[35] B.L. Adams, J. Kacher, EBSD-based microscopy: Resolution of dislocation density, CMC 14 (3) (2009) 185–196.

[36] A. Morawiec, Orientations and Misorientations, Springer Verlag, 2004.